

Experimental investigation of the dynamic stall phenomenon on a NACA 23012 oscillating airfoil

Alex Zanotti and Giuseppe Gibertini

Proc IMechE Part G:
J Aerospace Engineering
227(9) 1375–1388
© IMechE 2012
Reprints and permissions:
sagepub.co.uk/journalsPermissions.nav
DOI: 10.1177/0954410012454100
uk.sagepub.com/jaero



Abstract

An extensive experimental investigation was conducted on an oscillating NACA 23012 airfoil to study the flow structures and the consequent performances in dynamic stall conditions. The testing activity involved two different measurement techniques: fast unsteady pressure measurements and particle image velocimetry. The analysis of the experimental data set made possible to achieve a deep insight in the mechanism of the dynamic stall phenomena for the NACA 23012 airfoil in the different dynamic stall regimes. In particular, the flow velocity field measured on the airfoil upper surface described in detail the mechanism of the formation, migration and shedding of strong vortical structures characteristic of the deep dynamic stall. In addition, Gurney flap effects were investigated. The experimental results showed that it would be advantageous to deploy active Gurney flaps to improve helicopter rotor blade performances. The whole set of experimental results can be considered as a reference to validate computational fluid dynamics tools.

Keywords

Dynamic stall experiments, oscillating airfoil, particle image velocimetry, unsteady aerodynamics

Date received: 21 February 2012; accepted: 18 June 2012

Introduction

The strong demand for faster helicopters has spurred the aerodynamics research activity on new active blade design. The investigation of the dynamic stall phenomenon on the retreating blade represents one of the major topics in these projects. The main goal of the active blade would be the possibility to overcome the limitation of the performance induced by this phenomenon for classical helicopter rotor configurations.¹

In fact, the dynamic stall phenomenon occurs on the retreating rotor blades at high forward flight speed or during manoeuvres at high load factors, producing several adverse effects on the helicopter performance. The principal detrimental effects due to dynamic stall are: limitation of the forward speed and thrust; high control system loads; the introduction of a high level of vibrations affecting the helicopter dynamic performance in terms of manoeuvre capability and handling qualities; the occurrence of a single degree of freedom limit cycle oscillation called in literature ‘Stall Flutter’,² causing blade structural damage and excessive cabin vibration. The several negative effects on helicopter performance

and flight dynamics illustrates the dynamic stall importance in a more complete aerodynamic and aeroelastic analysis of the rotor and justifies the very large number of publications both in the numerical and experimental fields on this subject.

In fact, many recent activities analysed the effectiveness of different control systems integrated into the blade section in order to alleviate the detrimental effects of the dynamic stall phenomenon and to expand the helicopter flight envelope and vehicle utility. Currently, improvements in dynamic stall active control rely upon the optimisation of the blade airfoil shape³ or the use of blowing devices such as air-jet vortex generators⁴ or plasma actuators,⁵ that represent attractive solutions for the reduction of the airload hysteresis and the suppression of stall-driven flutter.²

Dipartimento di Ingegneria Aerospaziale, Politecnico di Milano, Italy

Corresponding author:

Alex Zanotti, Dipartimento di Ingegneria Aerospaziale, Politecnico di Milano, Campus Bovisio, Via La Masa 34, 20156 Milano, Italy.
Email: zanotti@aero.polimi.it

Furthermore, the research on dynamic stall is now focusing its attention on the evaluation of reliable modelling capabilities for the simulation of the phenomenon characterised by the rapid formation, migration and shedding of strong vortical structures, as in the case of deep dynamic stall regime.^{6,7} The validation of such numerical models necessitates of a thorough comparison between the simulation results and an experimental database, in particular for the deep dynamic stall conditions. With this aim, a new experimental rig was designed at Politecnico di Milano in order to test pitching blade section models in the wind tunnel. The design and performance of the experimental rig was purposely conceived to reproduce typical conditions of a full-scale retreating blade section (around the 75% of blade radius) in deep dynamic stall at high forward flight speed. The experimental rig involved two measurement techniques: fast unsteady pressure measurements (with Kulite transducers) and particle image velocimetry (PIV).

This article presents the main results of a comprehensive wind tunnel test campaign carried out on a NACA 23012 blade section. The NACA 23012 airfoil was selected since it has been employed both in the rotor blade design of several helicopters currently in operation and in experimental research activities carried out in the past years about the dynamic stall phenomenon on pitching blade sections.^{8,9}

The test activity produced a comprehensive set of experimental data through the two measurement techniques employed. The analysis of the experimental results was able to achieve a detailed insight of the different stages of the dynamic stall process for the NACA 23012 airfoil. The experimental analysis was completed by tests carried out overlaying a higher-order pitching motion to the sinusoidal motion of the blade model; this condition permitted the evaluation of elasticity effects of the rotor blades on the airloads in dynamic stall conditions.

Furthermore, a Gurney flap was tested to evaluate the effectiveness of this device for dynamic stall alleviation.

Experimental set-up

Wind tunnel and blade section model

The experimental activity was conducted at the Politecnico di Milano in the low-speed closed-return wind tunnel of the Aerodynamics Laboratory in the Aerospace Department. The wind tunnel has a rectangular test section with a height of 1.5 m and a width of 1 m. The maximum wind velocity is 55 m/s and the freestream turbulence level is less than 0.1%.

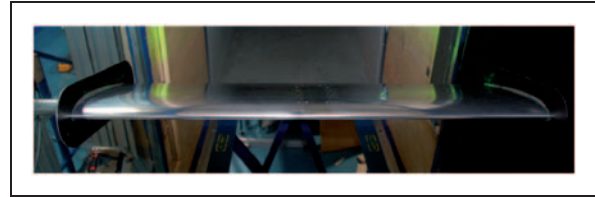


Figure 1. NACA 23012 blade section model inside the wind tunnel (PIV mode).



Figure 2. Motorised strut for the model pitching motion.

The aluminium machined airfoil model, with a chord $c = 0.3$ m and a span $b = 0.93$ m, has an interchangeable midspan section for the different measurement techniques employed, one for PIV flow surveys and another one for unsteady pressure measurement equipped with pressure taps positioned along the midspan chord line. The model is pivoted about two external steel shafts corresponding to 25% of the airfoil chord. End plates are mounted at the model extremity (Figure 1) to reduce the interference of the wind tunnel wall boundary layer and the extremity effects.

credo che questa considerazione renda valido l'uso di questo paper per la validazione di un caso 2D

Pitching motion rig

The model pitching motion is provided by a brushless servomotor with a 12:1 gear drive. The model is connected to the driving mechanism by a torsionally stiff steel laminae coupling between one of the external tubular shaft and the gear drive shaft (Figure 2).

Two encoders are directly mounted on the shaft on the other side of the model in respect to the motor: a

Penso che il NACA 23012 sia il profilo che dovremmo scegliere per il nostro progetto

Table 1. Pressure taps location on the NACA 23012 model midspan section.

Tap number	1	2	3	4	5	6	7
Location x/c	0	0.01	0.044	0.096	0.164	0.28	0.358
Tap number	8	9	10	11	12	13	14
Location x/c	0.453	0.618	0.76	0.9	0.9	0.767	0.628
Tap number	15	16	17	18	19	20	21
Location x/c	0.459	0.373	0.285	0.185	0.118	0.06	0.02

2048 imp/rev absolute digital encoder with EnDat 2.2 protocol is used for feedback control and a 4096 imp/rev incremental analogue encoder is used to get the instantaneous position of the model.

The model pitching motion is controlled by a proportional and derivative action using an interface software implemented in Labview.

Unsteady pressure measurement set-up

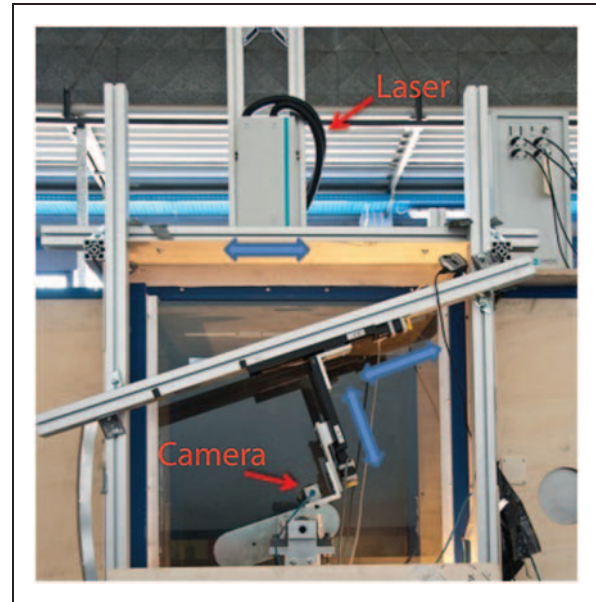
The time history of the lift and pitching moment during a pitching cycle was evaluated by the integration of the phase-averaged pressures. The phase average of the pressure signals was carried out using a bin of 0.1° angle-of-attack amplitude. The pressures were measured through 21 Kulite fast-response pressure transducers located inside the model interchangeable midspan section. The pressure transducers are positioned in a straight or L-shaped nylon machined pipe and sealed with a miniature rubber o-ring.

The locations of the pressure taps around the model midspan section are listed in Table 1 following a closed loop from the upper to the lower surface of the airfoil, starting from the leading edge.

The pressure transducer signals were acquired by a National Instrument compact data acquisition system equipped with six 24-bit A/D simultaneous bridge modules with four channels each. The pressure data from the transducers were acquired over 30 complete pitching cycles with a sampling rate of 50 kHz; the high sampling rate was suggested to capture the fine detail of the dynamic stall phenomenon characterised by severe unsteadiness conditions. The model angular position was measured simultaneously with the pressure transducer signals through the incremental encoder mounted directly on the model tubular shaft. The simultaneous acquisition of the encoder signals has been used for the evaluation of the phase-averaged airloads on a pitching cycle.

PIV set-up

The PIV system used a double-shutter CCD (charge-coupled device) camera with a 12-bit, 1280×1024 pixel

**Figure 3.** PIV set-up in the wind tunnel test section.

array and a 55 mm lens. The measurement area was composed by four $103 \times 82 \text{ mm}^2$ measurement windows spanning the airfoil chord direction, with a small overlapping between the adjacent windows. The choice to compose the complete observation field with smaller measurement windows was dictated by the will to obtain image pairs with a better resolution. The CCD camera was mounted on a dual axis traversing system driven by two stepper motors that allowed to move the measurement window along two orthogonal guides.

A Nd:Yag double-pulsed laser, with 200 mJ output energy and wavelength 532 nm, was positioned over the top of the test section (Figure 3) to illuminate the observation area through a slot in the wind tunnel roof. The laser was mounted on a single-axis traversing system in order to move the sheet along the wind tunnel flow direction. This solution allowed the use of a laser sheet with smaller width and a higher energy level centred on each measurement window.

A particle generator with Laskin nozzles was used for flow in-semination. The tracer particles, consisting of

small oil droplets with a diameter within the range 1–2 μm , were injected in correspondence of a section just after the fans and fulfill the wind tunnel volume with a homogeneous density.

The image pair post-processing was carried out using the PIVview 2C/3C software¹⁰ of PIVTEC. Multigrid technique¹¹ was employed to correlate the image pairs, starting from an interrogation window of 96×96 pixels to a window of 32×32 pixels. In order to filter out the effect of turbulent oscillations, the velocity flow fields were phase averaged over 40 image pairs.

Experimental results

Unsteady pressure measurements

Before the dynamic tests, a few static tests were carried out in order to validate the airloads measurement technique.

Figure 4 presents the static C_L - α curve measured at Reynolds number $Re = 1 \cdot 10^6$ (and corrected for two dimensional (2D) wind tunnel effects^{12,13}) compared with the curve measured by NACA¹⁴ at the same Reynolds number. The curves present a very good agreement in the total range of the considered angles of attack.

The main goal of the pressure measurements on the blade section model was the characterisation of the NACA 23012 airfoil performance in conditions typical of the flight envelope of a helicopter rotor in forward flight. With this aim, a comprehensive series of wind tunnel tests were carried out changing systematically the pitching cycle parameters such as the mean angle

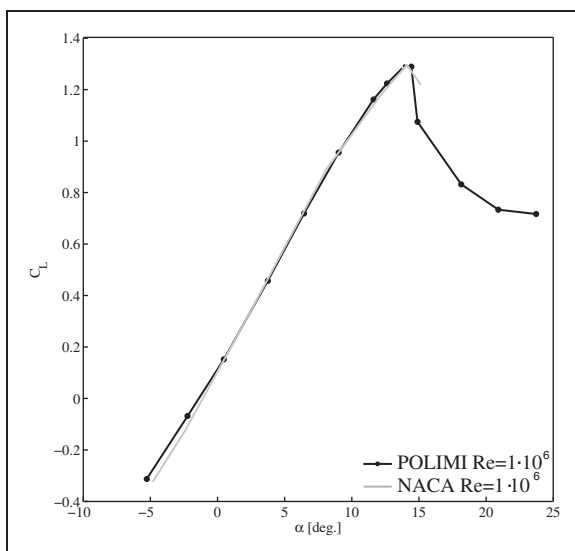


Figure 4. Comparison of steady C_L - α curves for NACA 23012 airfoil.

of attack, the oscillation amplitude and the reduced frequency. The set of tested conditions included 'Light Dynamic Stall' and 'Deep Dynamic Stall' conditions.¹ For example, the dynamic tests carried out at $k = 0.1$ with $Re = 1 \cdot 10^6$ ($Ma = 0.15$) reproduced the condition of a medium size helicopter retreating rotor blade section at about 75% radius in forward flight. The presented dynamic results are not corrected by the wind tunnel effects because well-established correction methods are not available for pitching airfoils, in particular for high oscillation amplitude pitching cycles.

Figure 5 presents the results of three tests reproducing different dynamic stall regimes obtained by increasing α_m from 6° to 15° with a constant pitching cycle oscillation amplitude equal to 10° and a constant reduced frequency equal to 0.1. The error bars on the curves represent the standard deviation of the measured airload coefficients.

In order to validate the present measurements, the curves were compared with the results of Leishman,⁸ obtained at a larger Reynolds number $Re = 1.5 \cdot 10^6$ ($Ma = 0.12$), because of the lack of available data at the same present Reynolds number. The results for $\alpha_m = 6^\circ$ and $\alpha_m = 10^\circ$ show a good agreement. The small differences of the curves may be due to the different Reynolds number but, beside this, could also be due to the fact that the two experimental set-up are not identical.⁸

Many physical features of the flow could be simply deduced by pressure measurements, taking into account the observation of other authors, as Leishman⁸ and McCroskey.¹ A more detailed observation was made possible by PIV but limited to $Re = 6 \cdot 10^5$ ($Ma = 0.09$) cases ('PIV flow surveys' section). In fact, the long run time required by the present PIV measurement would produce, at a higher velocity, a too long highly stressing load cycle on the model strut.

The test at $\alpha_m = 6^\circ$ corresponds to light dynamic stall regime because the maximum angle of attack is close to the static stall angle of attack. In this case (Figure 5(a)), the airload curves present a small amount of hysteresis as the flow is attached during most of the pitching cycle.

The pitching cycle conditions with higher mean angle of attack correspond to the deep dynamic stall regime. This regime is characterised by the vortex-shedding phenomenon and occurs when the maximum angle of attack is well above the static stall angle,¹⁵ as in the cases presented by Figure 5(b) and (c).

In particular, during the upstroke motion, lift grows linearly to a maximum value higher than the value obtained in static conditions, as the flow separation is delayed by a reduction in adverse pressure gradients on the airfoil upper surface produced by a kinematic induced camber effect due to the positive rapid pitching rate.¹⁵ For instance, in the test condition with $\alpha_m = 10^\circ$

qui sono presentate le differenze legate allo stallo dinamico leggero e forte

(Figure 5(b)), the measured lift coefficient grows linearly during almost all the upstroke motion as the flow remains attached to the airfoil upper surface. The lag of the flow reattachment process during the downstroke motion of the airfoil produced by the negative pitching rate produces the large hysteresis. In particular, the lift hump that occurs during the downstroke phase is a direct consequence of the migration of a strong vortex on the airfoil upper surface; this phenomenon represents a typical feature of the deep dynamic stall regime, as will be described by PIV flow surveys in the following section. In fact, the fast passage of a

strong vortical structure introduces a localised decrease of the pressure distribution on the airfoil upper surface, producing, consequently, the further increase of lift observed in the experimental curve. The mentioned change in pressure distribution occurring in this range of angles of attack is clearly visible in Figure 6(a) that shows the time history of the pressure coefficient C_p on the airfoil upper surface during the whole pitching cycle.

The severe unsteadiness conditions that characterise this phase of the pitching motion for the deep dynamic stall regime is also responsible of the large scatter of the

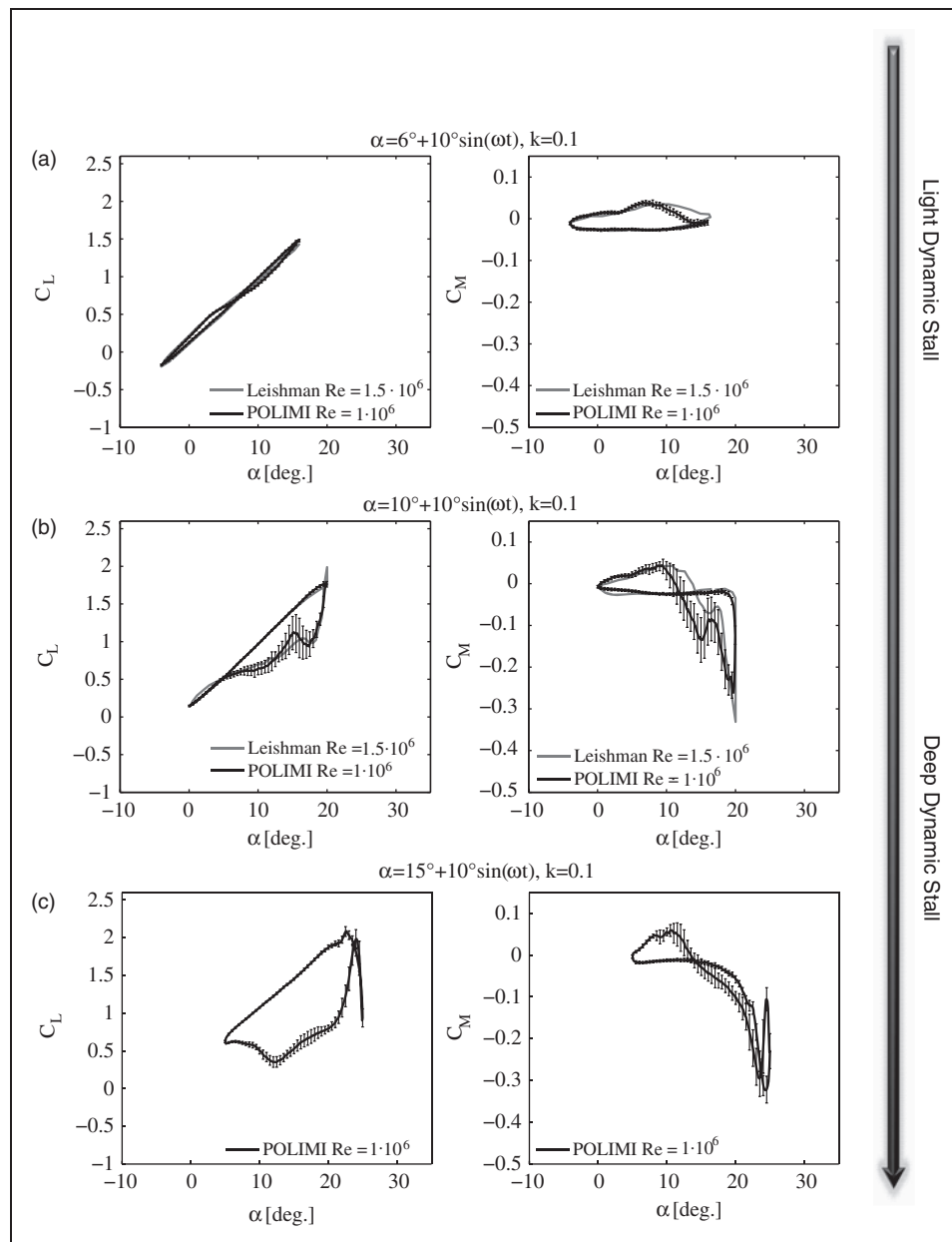
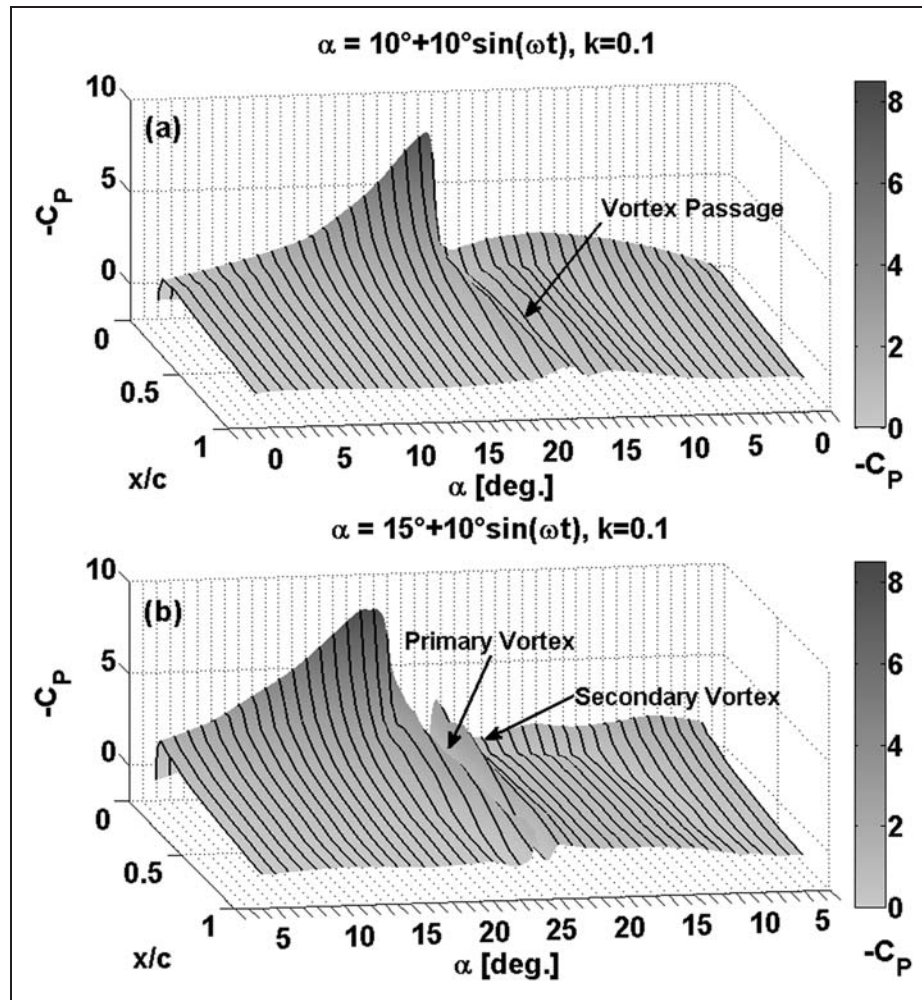


Figure 5. Lift and pitching moment curves measured for NACA 23012 at $Re = 1 \cdot 10^6$.



qui è possibile vedere il passaggio del vortice poiché al variare del tempo (che si traduce nella variazione dell'angolo di incidenza) osserviamo come ci sia un aumento di pressione che si sposta lungo la corda del profilo

potrebbe essere interessante mostrare questo tipo di grafico nel tempo per mostrare come riusciamo a cogliere anche noi questo vortice

Figure 6. Pressure coefficient time history on the NACA 23012 airfoil upper surface in deep dynamic stall conditions at $Re = 1 \cdot 10^6$.

measured airload coefficients, as observed for instance in the experiments by Gardner et al.¹⁶

Moreover, it has to be outlined that a net negative aerodynamic damping like this, produced by a higher area of C_M clockwise loop compared to the anticlockwise one, could lead to a condition of aeroelastic instability, the 'Stall Flutter' described by Carta.²

As observed in Figure 5(c), the airload curves for a pitching cycle characterised by a mean angle of attack close to the airfoil static stall angle of attack presents a typical behaviour, in the last part of the upstroke motion, due to the formation, on the airfoil upper surface, of a vortical structure called 'Dynamic Stall Vortex' (DSV).^{1,15} The change in pressure distribution over the airfoil upper surface due to the DSV migration produces a non-linear change of the C_L - α curve slope from $\alpha = 20^\circ$ to $\alpha = 23^\circ$. In addition, the vortex sweep over the airfoil produces an aft movement of the centre of pressure and, consequently, a significant increase in

nose-down pitching moment. Another interesting effect due to the DSV migration is the delay of the pitching moment break (about $\alpha = 20^\circ$) in respect to the lift stall (about $\alpha = 23^\circ$); in fact, the pitching moment break starts at the stage of the vortex formation, while the lift stall occurs when the vortex leaves the airfoil passing into the wake. The stage of vortex shedding at about $\alpha = 24^\circ$ is accompanied by a rapid overshoots of lift and pitching moment. At the beginning of the downstroke motion, the airload curves present secondary peaks of lift and pitching moment due to the formation and travelling of a secondary vortex. For this last test condition, the effects of the convection of two vortices on the airfoil upper surface pressure distribution are clearly visible in Figure 6(b). The primary vortex formation starts at about $\alpha = 21^\circ$ (upstroke), producing a trailing edge pressure divergence when it is leaving the airfoil. The secondary vortex formation starts at the beginning of the downstroke motion

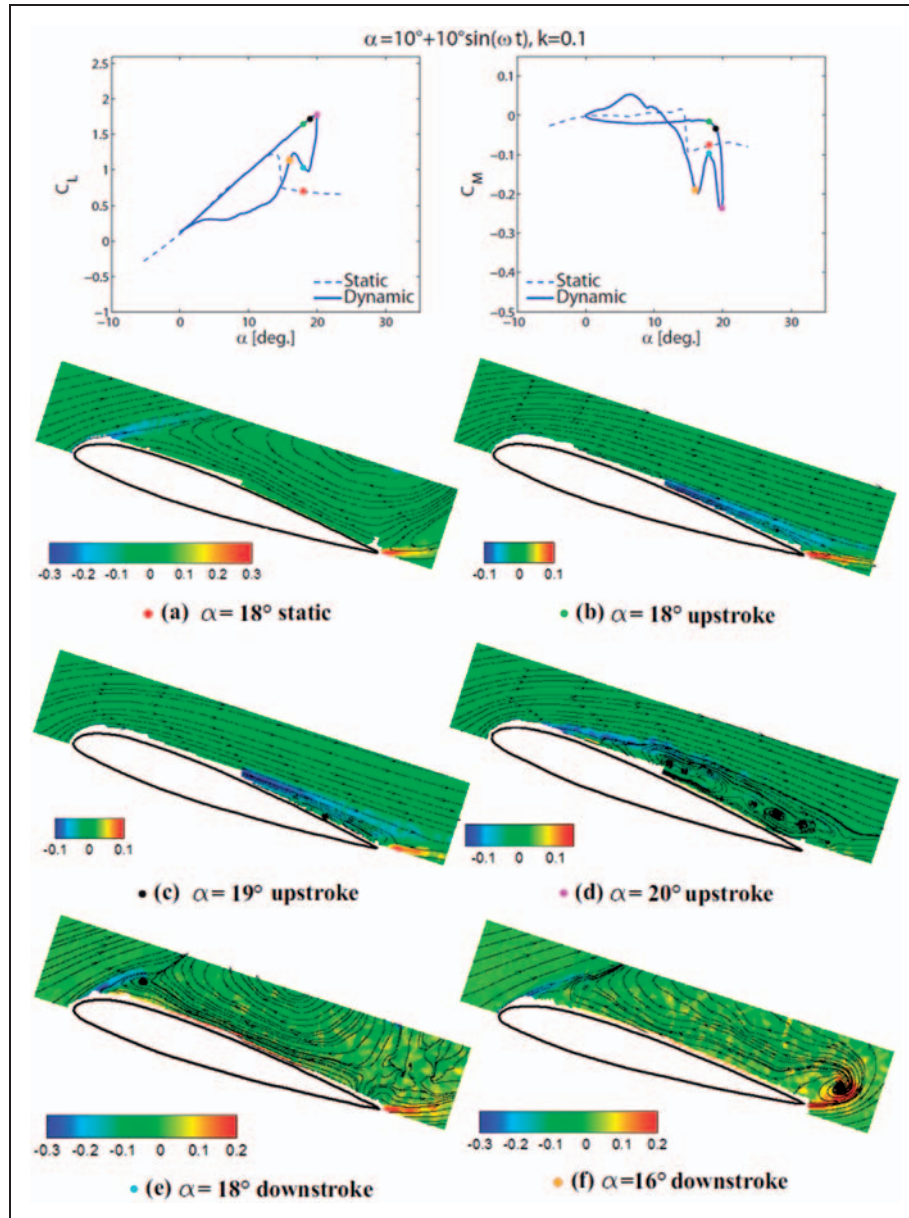


Figure 7. NACA 23012 PIV flow surveys and airload curves measured for $\alpha(t) = 10^\circ + 10^\circ \sin(\omega t)$ at $Re = 6 \cdot 10^5$, deep dynamic stall condition; colours referred to vorticity levels normalised by the maximum value.

(about $\alpha = 24^\circ$). Observing the evolution of the pressure distribution on the airfoil, it can be deduced that the secondary vortex travels faster than the primary one.

The results of the pressure measurements carried out to evaluate the influence of mean angle of attack increase on pitching airfoil performance are in quite good agreement with the experimental studies carried out by Krzysiak¹⁷ and Wood¹⁸ with a similar test equipment for a pitching NACA 0012 airfoil; in particular, both the airload hysteresis amount for the different dynamic stall regimes and the effects of DSV formation on the airload curves behaviour present the

same characteristic features observed in the results presented in these works.

PIV flow surveys

For two pitching cycle conditions typical of the deep dynamic stall regime, PIV flow surveys carried out on the airfoil upper surface allowed to get a more detailed insight. In particular, the pitching cycle conditions selected for the PIV surveys consist of two sinusoidal pitching cycles with $\alpha_m = 10^\circ$ or $\alpha_m = 15^\circ$, $\alpha_a = 10^\circ$ and $k = 0.1$. The wind tunnel velocity was $U_\infty = 30$ m/s

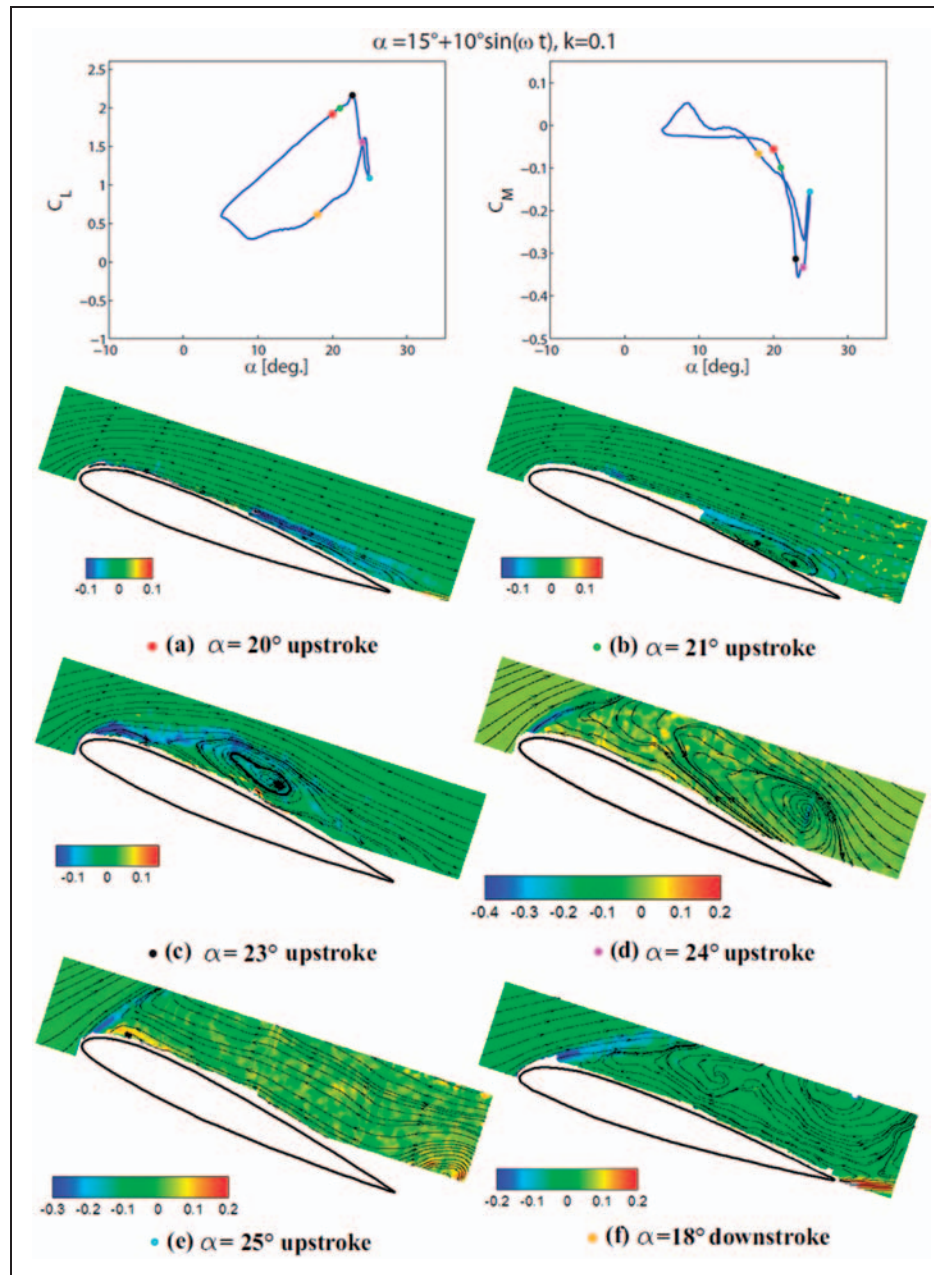


Figure 8. NACA 23012 PIV flow surveys and airload curves for $\alpha(t) = 15^\circ + 10^\circ \sin(\omega t)$, $k=0.1$ at $Re = 6 \cdot 10^5$, deep dynamic stall condition; colours referred to vorticity levels normalised by the maximum value.

corresponding to $Re = 6 \cdot 10^5$ and $Ma = 0.09$. Figures 7 and 8 present a series of pictures illustrating, for the different cases, the flow field measured at different angles of attack, both in upstroke and downstroke. The measured flow field is represented by the vorticity of the velocity field contours and by instantaneous streamlines. Airload curves are also included in Figures 7 and 8 and it can be observed that the lift and pitching moment curves present the same behaviour of the curves measured at the higher Reynolds number $Re = 1 \cdot 10^6$ (compare Figure 5), so that it can

be reasonably assumed that the main aerodynamic phenomena are the same at the two Reynolds numbers.

In the first case considered ($\alpha_m = 10^\circ$), in order to show the differences between steady and oscillating conditions, a preliminary steady PIV survey was carried out for still airfoil at $\alpha = 18^\circ$ (corresponding to a post-stall condition). The flow field in static post-stall condition presents a complete separation of the flow on the airfoil upper surface starting from the leading edge (see Figure 7(a)). In dynamic conditions, at the same incidence in upstroke motion, the flow is fully attached to

come
spiegavano
prima con la piv
non si poteva
usare un Re
troppo
alto altrimenti
con alpha medio
di 15 gradi si
spaccava fuori
tutto

the airfoil upper surface, as the stall is delayed at a higher angle of attack by the effect of the rapid positive pitching rate.

In fact, in the dynamic condition with $\alpha_m = 10^\circ$, the flow on the airfoil upper surface is attached for almost all the upstroke motion, in particular, from $\alpha = 0^\circ$ to $\alpha = 18^\circ$, and the lift coefficient is also linearly increased. From $\alpha = 18^\circ$, the flow separation starts at the airfoil trailing edge region; in particular, as shown by the vorticity field in Figure 7(b) and (c), the separated flow at $\alpha = 18^\circ$ and 19° extends over about 50% of the airfoil chord. The separated flow region grows towards the leading edge as the airfoil reaches the maximum angle of attack at $\alpha = 20^\circ$ and is characterised by the formation of small vortices within the shear layer (Figure 7(d)); at this stage, lift and nose-down pitching moment coefficients reach their maximum peak.

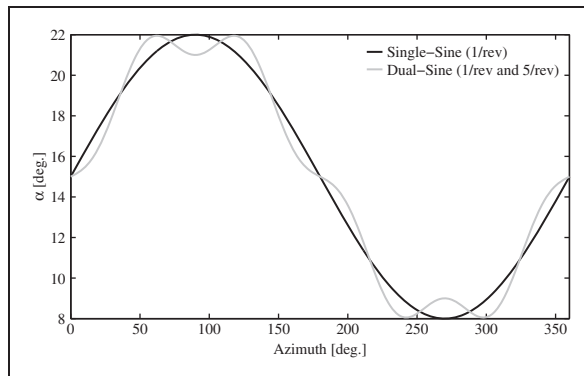


Figure 9. Comparison of the tested dual-sine higher-order pitching motion and single-sine pitching motion.

During the downstroke motion, the flow presents a wide separation on the airfoil upper surface and is characterised by the formation and migration of strong vortices. For instance, in the range between $\alpha = 18^\circ$ and $\alpha = 16^\circ$ in downstroke (Figure 7(e) and (f)), the PIV measurements show the passage of large vortices on the airfoil upper surface. In particular, the flow field at $\alpha = 18^\circ$ in downstroke illustrated in Figure 7(e) presents a small vortex near the leading edge and an extended one at about half of the chord. At $\alpha = 16^\circ$ in downstroke, the vorticity field in Figure 7(f) clearly shows a strong vortex detaching the trailing edge. The large low-speed recirculating flow region on the upper surface recalls air from the airfoil lower surface, causing the formation of this counterclockwise vortex located very close to the trailing edge. As mentioned in the previous section, the passage of such strong vortical structures is responsible of the airload hump observed in this phase of the motion.

Moreover, during the downstroke motion, when the flow field is characterised by severe unsteadiness conditions, 3D effects on the flow field could be considered not negligible. These 3D flow features could be in part due to the intrinsic 3D nature of dynamic stall but they could also be related to the use of a finite-span model and to the wind tunnel side walls. No experimental PIV surveys or unsteady pressure measurements are available along spanwise direction due to the actual test setup. Nevertheless, further considerations about 3D effects could be deduced by the comparison of the experimental data with the results of computational fluid dynamics (CFD) simulations carried out using a 3D numerical model reproducing the experiments; this is the main goal of the activity currently ongoing at Politecnico di Milano.

problemi legati alla natura 3D della prova

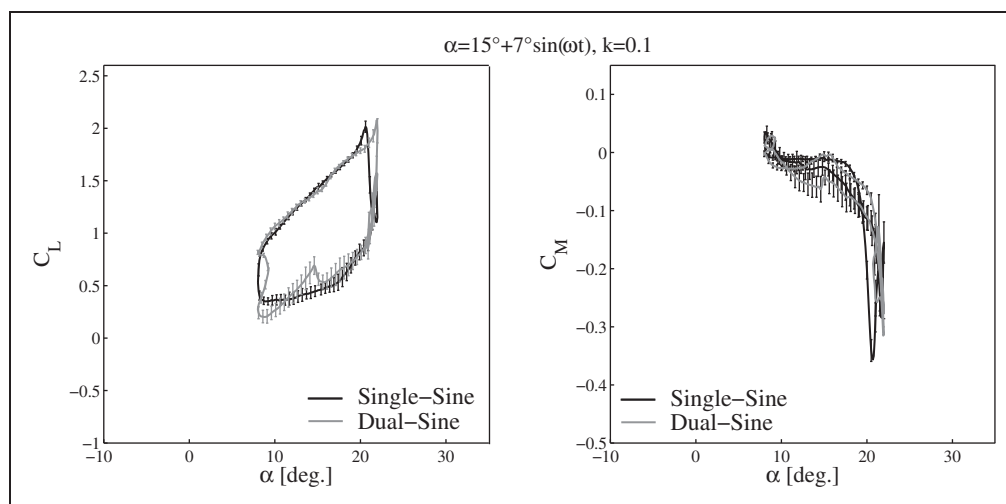


Figure 10. Comparison of airload curves measured for NACA 23012 with single- and dual-sine pitching motions at $Re = 4 \cdot 10^5$.

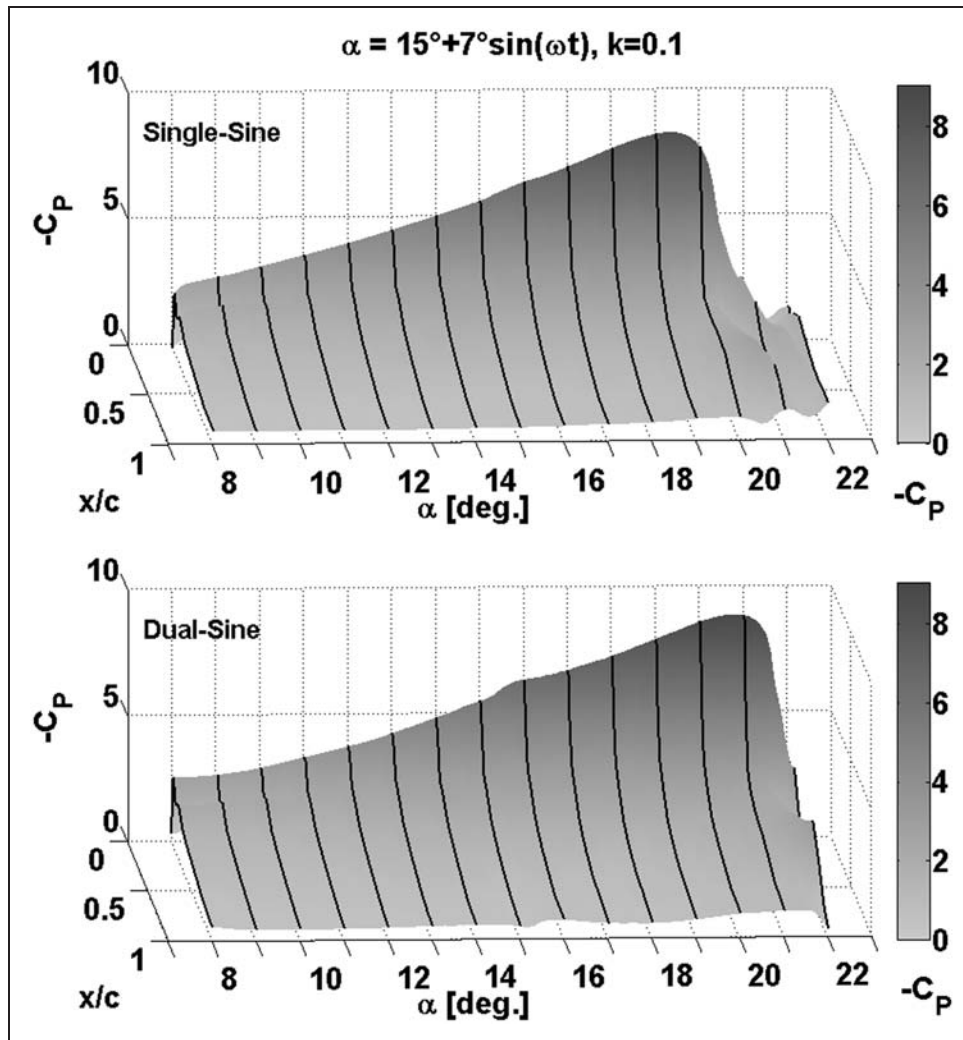


Figure 11. Comparison of the pressure coefficient time history on the NACA 23012 airfoil upper surface for the single- and dual-sine pitching motions at $Re = 4 \cdot 10^5$.

In the dynamic condition with $\alpha_m = 15^\circ$, the PIV flow surveys at the higher angles of attack of the upstroke motion illustrate the DSV formation (Figure 8).

In Figure 8(a), ($\alpha = 20^\circ$) the flow separation start at the trailing edge is clearly visible and the vorticity field shows the extension of the separated flow region. Then, Figure 8(b) ($\alpha = 21^\circ$) shows the start of the DSV structure formation. At $\alpha = 23^\circ$, as can be observed in Figure 8(c), the DSV reaches the midchord and extends over about the 50% of the airfoil upper surface; the vorticity field for this condition shows small vortical structures inside the clockwise rotating DSV, as observed in Raffel's et al.¹⁹ experiments for a NACA 0015 airfoil pitching with the same motion law. Increasing the angle of attack, the DSV grows, moves downstream and eventually, leaves the airfoil, as shown

in Figure 8(d) for $\alpha = 24^\circ$. The change of the pressure distribution on the airfoil upper surface due to the formation of this vortex disturbance produces the non-linear increase of the lift coefficient curve slope and the break of the nose-down pitching moment that increases rapidly as the DSV moves on the airfoil upper surface.

At the maximum incidence of the oscillating cycle, $\alpha = 25^\circ$, where the airfoil reverses the pitching motion, the DSV has definitively left the airfoil and a small counterclockwise vortical structure can be observed at the trailing edge (Figure 8(e)). The flow on the airfoil upper surface is fully separated and the reversed flow region is extended over the entire airfoil chord. The random-like distribution of small-scale vortical structures shown within the separated flow region in

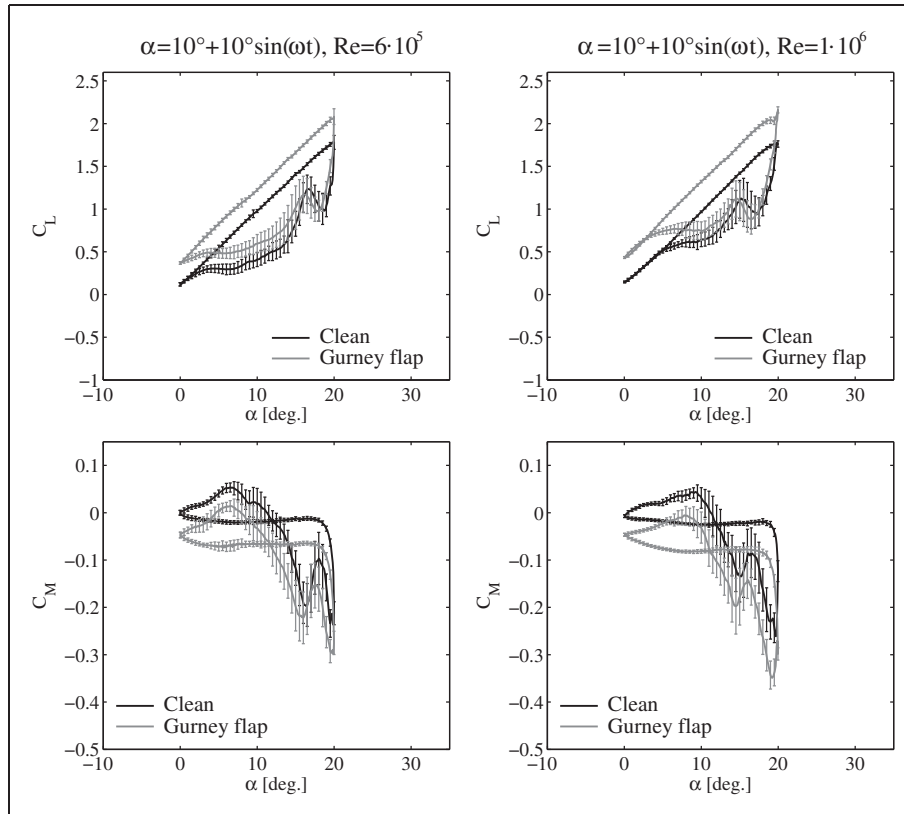


Figure 12. Comparison of airload curves measured for NACA 23012 airfoil equipped with a Gurney flap.

Figure 8(d) and (e) could be explained by a certain level of noise in the measured data.

For the whole downstroke motion, the flow field on the airfoil upper surface is fully separated, as can be observed, for instance, at $\alpha = 18^\circ$ in Figure 8(f). The different behaviours of the flow topology observed during the motion of upstroke and downstroke explain the large amount of airloads hysteresis.

Higher-order pitching motion

In order to complete the characterisation of the NACA 23012 performance in dynamic stall conditions, a higher-order pitching motion overlaid to the sinusoidal motion of the airfoil was tested, as in Gardner's et al.¹⁶ experiment. The goal of this activity was to evaluate the effects on the local angle of attack produced by a 5/rev oscillation, possibly due to the elasticity of the blades or to active vibration control systems.

In particular, the following dual-sine pitching motion was tested for the NACA 23012 airfoil to compare the measured airloads to the single-sine pitching motion law

$$\alpha(t) = 15^\circ + 7^\circ \sin(\omega t) - 1^\circ \sin(5 \times (\omega t)) \quad (1)$$

at a reduced frequency $k = 0.1$ and $Re = 4 \cdot 10^5$. Figure 9 presents the shape of the tested dual-sine pitching law.

As it can be observed from Figure 9, the two pitching motion laws share the same maximum and minimum angle of attacks.

Figure 10 presents the comparison of the measured lift and pitching motion coefficients for the single- and dual-sine pitching motions.

In the dual-sine case, the separation and the stall are delayed to a higher angle of attack in comparison to the single-sine case, as the angular velocity of the pitching airfoil in upstroke is higher around the separation angle of attack. This increases the kinematic effect of induced camber, producing a further delay of the dynamic stall. This phenomenon can be explained by the comparison of the C_p time history measured on the airfoil upper surface during the upstroke motion. In fact, as can be clearly observed from Figure 11, for the dual-sine case, the suction pressure peak is higher than in the single-sine case and drops at a higher angle of attack.

An other interesting result about the effects of the dual-sine pitching motion concerns the pitching moment coefficient; in particular, the peak of the pitching moment coefficient occurs at the maximum angle of attack and presents about a 11% reduction in comparison to the single-sine case.

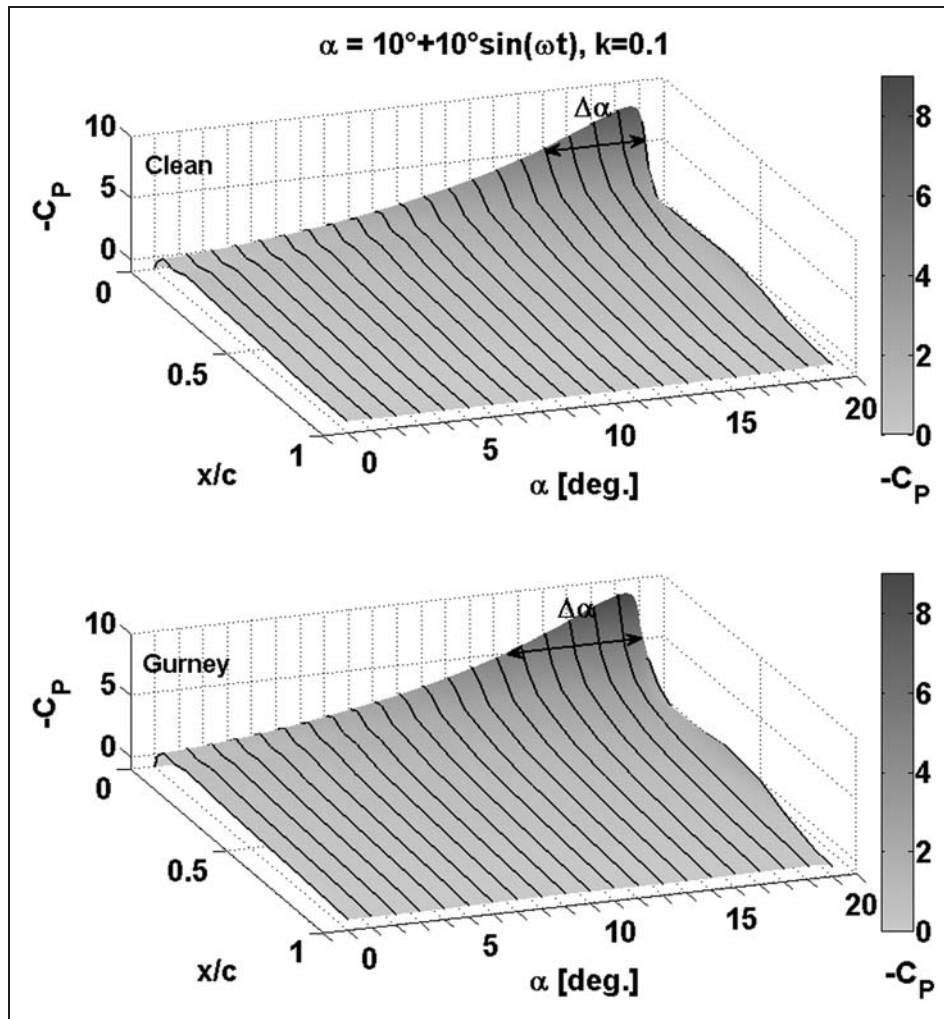


Figure 13. Comparison of the pressure coefficient time history on the NACA 23012 airfoil upper surface with and without a Gurney flap.

Experimental activity on Gurney flap effects

The comprehensive experimental activity on the NACA 23012 airfoil was completed by a test campaign carried out to evaluate the effects of a Gurney flap for dynamic stall alleviation. In particular, a Gurney flap made in carbon fibre was attached at the airfoil trailing edge of the NACA 23012 blade model protruding with 4 mm height downwards.

Figure 12 presents the comparison between the airloads measured with and without the Gurney flap in the case with $\alpha_m = 10^\circ$, $\alpha_a = 10^\circ$ and $k = 0.1$ at two different Reynolds numbers, $Re = 6 \cdot 10^5$ and $Re = 1 \cdot 10^6$.

As it can be observed from the test results, the Gurney flap introduces a remarkable effect consisting of a shift of the lift and pitching moment curves in comparison to the clean airfoil condition. In particular, the increase of the lift coefficient occurs during all the upstroke motion (about 15% lift enhancement near the

maximum C_L) analogously to what happens in steady applications and in agreement with the results of Chandrasekhara et al.²⁰ for a pitching VR-12 airfoil. This can be considered an appreciable effect for the retreating blade performance, due to the associated higher level of available thrust.

The pressure distribution measured on the airfoil upper surface during the upstroke motion explains the reason for the increase in lift coefficient due to the Gurney flap. Figure 13 presents the comparison of the C_p time history measured with and without the Gurney flap for the pitching cycle at $Re = 6 \cdot 10^5$; the angle of attack range where the $-C_p$ contour levels are above five is indicated with $\Delta\alpha$. For the configuration with the Gurney flap, the peak pressures over the airfoil upper surface are higher and spread over a larger angles of attack range, leading to the production of a sensible higher lift level respect to the clean airfoil configuration, even at higher angles of attack.

The observation of the moment coefficient curve confirms that advantages can be obtained by the use of an active Gurney flap, as proposed by several authors.^{21,22} In particular, the fact that the Gurney flap produces a negative offset either in upstroke and downstroke suggests that retreating the Gurney flap in downstroke could increase the counterclockwise loop area (positive aerodynamic damping) and reduce the clockwise loop area (negative dumping), reducing the risks of stall flutter occurrence.

Conclusions

A detailed insight of the typical features involved in the dynamic stall phenomenon for a NACA 23012 airfoil was obtained through a comprehensive experimental campaign. The experimental rig designed for testing pitching blade section models enabled to reproduce the typical conditions of the flight envelope of a full-scale retreating rotor blade section at high forward flight speed. The use of both fast pressure transducers and PIV allowed to relate the load distributions to the flow phenomena. In fact, the PIV flow field surveys, performed with a high spatial resolution, illustrated the detailed flow physics that characterise the different phases of the blade stall process and in particular the formation of the DSV typical of the deep dynamic stall regime.

The comprehensive data set produced by the experimental activity could be considered as a reference data base for the validation of numerical models. In fact, an ongoing activity at Politecnico di Milano is evaluating the modelling capabilities for this peculiar flow conditions comparing different 2D and 3D CFD models against the experimental results presented in this study, in particular for the deep dynamic stall condition.

The test with a Gurney flap demonstrated an appreciable effect on the airfoil performance and demonstrated that a cyclically deployed Gurney flaps could be used to improve the helicopter main rotor performances. In particular, these results suggest that the flap has to be deployed downward during the upstroke phase (retreating blade) and retreated in the downstroke phase (advancing blade) in order to increase the retreating blade lift and, at the same time, to reduce the risk reduction of stall flutter occurrence. Hence, the results obtained from the experiments with the fixed Gurney flap encourage the research activity on the use of an active Gurney flap for dynamic stall control purposes. An other interesting topic that should be further investigated is about the effects of higher-order pitching motion. A preliminary test carried out in this study (similarly to what done by Gardner et al.¹⁶) has

shown sensible effects for a 1° 5/rev oscillation superimposed to the main 1/rev oscillation.

Funding

This research was carried out under the sponsorship of the Dipartimento di Ingegneria Aerospaziale, Politecnico di Milano, Italy.

References

1. McCroskey WJ. The Phenomenon of dynamic stall. NASA TM 81264, 1981.
2. Carta FO. An analysis of the stall flutter instability of helicopter rotor blades. *J Am Helicopter Soc* 1967; 12: 1–8.
3. Chandrasekhara M, Martin P and Tung C. Compressible dynamic stall control using a variable droop leading edge airfoil. *J Aircr* 2004; 41: 862–869.
4. Singh C, Peake D, Kokkalis A, et al. Control of rotorcraft retreating blade stall using air-jet vortex generators. *J Aircr* 2006; 43: 1169–1176.
5. Post M and Corke T. Separation control using plasma actuators: dynamic stall vortex control on oscillating airfoil. *AIAA J* 2006; 44: 3125–3135.
6. Visbal MR. Numerical investigation of deep dynamic stall of a plunging airfoil. *AIAA J* 2011; 49: 2152–2170.
7. Costes M, Richez F, Le Pape A, et al. Numerical investigation of three dimensional effects during dynamic stall. In: *37th European rotorcraft forum*, Gallarate (VA), Italy, 13–15 September 2011.
8. Leishman JG. Dynamic stall experiments on the NACA 23012 aerofoil. *Exp Fluids* 1990; 9: 49–58.
9. Raffel M, Kompenhans J, Stasicki B, et al. Velocity measurement of compressible air flows utilizing a high-speed video camera. *Exp Fluids* 1995; 18: 204–206.
10. PIVTEC. PIVview 3C version 3.0, user manual, <http://www.pivtec.com>.
11. Raffel M, Willert C and Kompenhans J. *Particle image velocimetry, a practical guide*. Heidelberg: Springer, 1998.
12. Barlow JB, Rae WH and Pope A. *Low-speed wind tunnel testing*. Chichester: John Wiley & Sons Inc., 1999.
13. Maskell EC. *A theory of blockage effects on bluff bodies and stalled wings in a closed wind tunnel*. British ARC R & M 3400, 1965.
14. Loftin Jr LK and Smith HA. Aerodynamic characteristics of 15 NACA airfoil sections at seven Reynolds numbers. NACA Technical Report, Langley Aeronautical Laboratory, 1949.
15. Leishman JG. *Principles of helicopter aerodynamics*. Cambridge Aerospace Series. Cambridge: Cambridge University Press, 2000.
16. Gardner AD, Richter K, Mai H, et al. Experimental investigation of dynamic stall performance for the EDI-M109 and EDI-M112 airfoils. In: *37th European rotorcraft forum*, Gallarate (VA), Italy, 13–15 September, 2011.
17. Krzysiak A. Experimental investigation of a dynamic stall on the oscillating NACA 0012 airfoil. *Trans Inst Aviation* 2006; 4: 1–52.

18. Wood ME. *Results from oscillatory pitch tests on the NACA 0012 blade section*. Aircraft Research Association. Bedford, UK, ARA Memo 220, 1979.
19. Raffel M, Kompenhans J and Wernert P. Investigation of the unsteady flow velocity field above an airfoil pitching under deep dynamic stall conditions. *Exp Fluids* 1995; 19: 103–111.
20. Chandrasekhara M, Martin P and Tung C. Compressible dynamic stall performance of a variable droop leading edge airfoil with a Gurney flap. *J Am Helicopter Soc* 2008; 53: 18–25.
21. Min B, Sankar LN, Rajmohan N, et al. Computational investigation of gurney flap effects on rotors in forward flight. *J Aircr* 2009; 46: 1957–1964.
22. Yeo H. Assessment of active controls for rotor performance enhancement. *J Am Helicopter Soc* 2008; 53: 152–163.

Appendix

Notation

b	blade section model span
c	blade section model chord
C_L	lift coefficient
C_M	pitching moment coefficient about the airfoil quarter chord
C_P	pressure coefficient
f	airfoil oscillation frequency
k	reduced frequency = $\pi fc/U_\infty$
Ma	Mach number
Re	Reynolds number
U_∞	freestream velocity
α	angle of attack (°)
α_a	pitching oscillation amplitude (°)
α_m	mean angle of attack (°)
ω	circular frequency (rad/s)